
Investigation of Fe isotope systematics for the complete sequence of natural and metallurgical processes of Ni lateritic ores: Implications for environmental source tracing

Ratié Gildas ^{1,*}, Garnier Jérémie ², Vieira Lucieth Cruz ², Ferreira Araujo Daniel ³, Komárek Michael ¹, Poitrasson Franck ⁴, Quantin Cécile ⁵

¹ Department of Environmental Geosciences, Faculty of Environmental Sciences, Czech University of Life Sciences Prague, Kamýcká 129, 165 00, Prague - Suchdol, Czech Republic

² UnB, IG/GMP-ICC Centro, Campus Universitário Darcy Ribeiro, 70910-970, Brasília-DF, Brazil/Laboratoire Mixte International "Observatoire des Changements Environnementaux" (LMI OCE), Institut de Recherche pour le Développement, University of Brasília, Campus Darcy Ribeiro, Brasília, Brazil

³ Laboratoire de Biogéochimie des Contaminants Métalliques, Ifremer, Centre Atlantique, F44311, Nantes Cedex 3, France

⁴ Laboratoire Géosciences Environnement Toulouse, UMR 5563 CNRS-UPS-IRD-CNES, 14-16, avenue Edouard Belin, 31400, Toulouse, France

⁵ UMR 8148 GEOPS, Université Paris-Saclay – CNRS, 91405, Cedex, France

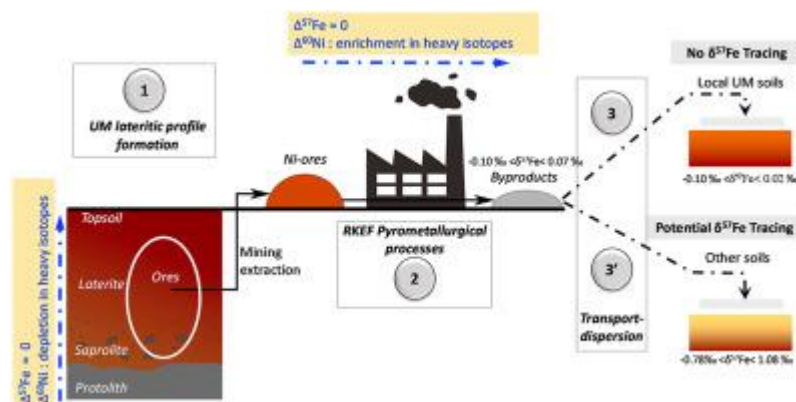
* Corresponding author : Gildas Ratié, email address : ratie@fzp.czu.cz

Abstract :

Metal isotopes are versatile pollutant source trackers, but biogeochemical processes can overprint or alter the original source isotopic fingerprint and thus hinder contamination tracing. Here, we explore Fe isotope systematics for the complete range of natural and metallurgical processes related to Ni lateritic ores from Barro Alto, Brazil, to assess its potential as a tracer in polluted lateritic soil contexts developed in an ultramafic system.

The homogeneous $\delta^{57}\text{Fe}$ values from protolith to soil confirmed that no significant Fe isotopic variation occurred during the formation of the deep lateritic profile. In addition, no Fe isotopic fractionation was found during the smelting process. Although the $\delta^{57}\text{Fe}$ values resulting from mining activities fall within the range of terrestrial sample signatures, the conservation of the $\delta^{57}\text{Fe}$ values from the ores to the by-products is an advantage for tracing anthropogenic sources when (i) the pyrometallurgical plant uses feeding material with Fe ores imported from other geological formations exhibiting different $\delta^{57}\text{Fe}$ values and/or (ii) the by-products are transported or dispersed to other locations with different $\delta^{57}\text{Fe}$ signatures in the topsoil.

Graphical abstract



Highlights

► Fe mobility does not induce isotopic fractionation during chemical weathering. ► There is no evidence of Fe isotope fractionation during the RKEF smelting process. ► Smelting slags are stamped with $\delta^{57}\text{Fe}$ values from Ni laterite ores. ► The use of Fe isotopes as an environmental tracer in lateritic soils is limited. ► Fe isotopes may be a potential tracer of mining activities in non-lateritic soils.

Keywords : metal cycle, iron isotopes, laterite, chemical weathering, smelting process

40 **1. Introduction**

41 The increasing global demand for metals has led to intense mining activities and their consequent
42 remobilization and enrichment in surface compartments, notably soils (Nriagu and Pacyna, 1988; Rauch
43 and Pacyna, 2009). Of particular concern is the soil contamination associated with metal extraction from
44 saprolite ores, such as the extraction of Ni, where its concentration of approximately 3 wt% implies high
45 economic value (Butt and Cluzel, 2013). However, in recent decades, limonitic ore (i.e., metals associated
46 with Fe oxyhydroxides) refining has increased as a result of the application of modern technologies
47 (allowing better yield recovery). In that ore, Fe contents can reach 40 wt% and Ni can occur in
48 concentrations of up to 1 wt% in Fe oxides (primarily hematite and goethite) (Manceau et al., 2000;
49 Quantin et al., 2002; Dublet et al., 2012 and 2015, Ratié et al., 2018). Smelting processes such as the

50 rotary kiln-electric furnace (RKEF) process are used to extract Ni from mixtures of saprolite and limonite
51 ores, yielding crude ferronickel (FeNi) composed of approximately 70% Fe and 30% Ni (Crundwell et al.,
52 2011). In the feeding material, Fe is primarily present as Fe(III) in Fe oxides and Fe(II)/Fe(III) in the
53 saprolite (e.g., smectite-type, serpentine, pyroxene, spinel, olivine). The by-products of the ore refining
54 process, i.e., fly ash and slag wastes, are Si-, Fe- and Mg-rich materials.

55 Generally, the pyrometallurgical wastes are either stored in the surrounding environment in
56 settling ponds (fly ash), dumped (slags), or partially reprocessed for metal recovery (fly ash). Such
57 disposal sites are susceptible to rainfall leaching and wind remobilization that can lead to the
58 contamination of the superficial environment and pose major risks to public health (Ettler et al., 2018).
59 The release of metals in soils by leaching is highly time-dependent (Barna et al., 2004; Bril et al., 2008;
60 Seignez et al., 2008; Ettler and Johan, 2014) and increases when slag disposal sites are flooded and/or
61 occurs in water-saturated environments (Ganne et al., 2006; Navarro et al., 2008; Houben et al., 2013).
62 Thus, understanding the dynamics of metals at contaminated sites, i.e., their sources, pathways and sinks,
63 is of the highest priority to develop effective environmental management and monitoring programs.

64 For that purpose, the use of metal isotopic signatures can be useful in the identification and
65 quantification of contaminant sources and for understanding how biogeochemical processes affect
66 contaminant transport (Bullen, 2014; Wiederhold, 2015). The primary challenge to successfully applying
67 isotopes as environmental tracers is to identify isotopic signatures that are distinctive between
68 anthropogenic and natural materials and to deconvolve the original isotopic signal from subsequent
69 isotopic fractionations induced by biogeochemical processes. In the case of stable isotopes of Zn and Cd,
70 industrial or metallurgical fractionation during ore refining results in manufactured products and by-
71 products that are isotopically distinct from their natural sources (e.g., Mattielli et al., 2006; Kavner et al.,
72 2008; Sivry et al., 2008; Sonke et al., 2008; Shiel et al., 2010; Chrastný et al., 2016; Klein and Rose,
73 2020). In contrast, Cu and Ni show little or no stable isotope fractionation during ore refining by smelting
74 due to their high boiling points (Bigalke et al., 2010; Ratić et al., 2016). As a consequence, the

75 manufactured metals, slags and other metallurgical by-products have an isotopic signature similar to that
76 of the ore concentrates. In soil pollution contexts, overlaps between ore and natural background isotope
77 compositions may compromise source tracking (Ratié et al., 2016; Šillerová et al., 2017). To overcome
78 this drawback, the coupling of two stable metal isotope systems has been used to enhance source
79 discrimination and deconvolution of the different biogeochemical processes involved in acid-mine mining
80 (Borrok et al., 2009), coastal systems (Araújo et al., 2019a, b) and urban atmospheres (Souto-oliveira et
81 al., 2017, 2018).

82 In this work, we explore Fe isotope systematics in lateritic soils from an ultramafic system and the
83 associated Ni ores refined in a pyrometallurgical system in Barro Alto, Brazil. Previously, an analogous
84 study was conducted to investigate Ni isotopes, which demonstrated a low level of Ni isotope
85 fractionation during ore refining that did not allow the use of Ni isotopes as tracers of contamination
86 (Ratié et al., 2016). Here, we attempt to gain new insights by using Fe isotopes, which have never been
87 explored in this context despite their potential. In contrast to Ni, Fe is redox-sensitive. Its solid speciation
88 differs from the Ni-bearing phases in the lateritic profile, and it occurs at an order of magnitude higher
89 concentrations.

90 Iron isotopes demonstrate special features of fractionation, both abiotically and biotically induced
91 in natural and anthropic materials, that can be useful in our case study (Dauphas et al., 2017; Wu et al.,
92 2019). As demonstrated by Poitrasson et al. (2008) for chemical weathering in Cameroon, the
93 lateritization process, which occurs over several million years, results in almost no $\delta^{57}\text{Fe}$ variation. This
94 feature was subsequently confirmed on other laterites from China and the Philippines, the latter being
95 developed on peridotites (Liu et al., 2014; Li et al., 2017). In contrast, modern soil studies from both
96 temperate and tropical areas and even Paleoproterozoic laterites showed much more significant Fe isotopic
97 variation (Fante and Depaolo, 2004; Emmanuel et al., 2005; Thompson et al., 2007; Wiederhold et al.,
98 2007; Yamaguchi et al., 2007; Fekiacova et al., 2013; Akerman et al., 2014). A key driving factor was the
99 separation of two iron pools having different iron redox states, and therefore contrasted Fe isotope

100 signatures (Wu et al., 2019). Iron isotope systematics was also successfully used to fingerprint
101 anthropogenic and natural sources in river sediments (Chen et al., 2014) in an alpine watershed impacted
102 by acid mine drainage (Borrok et al., 2009; Herbert Jr and Schippers, 2008). Iron isotopes were also used
103 to trace anthropogenic combustion through the collection of aerosols from sources in the Sahara, North
104 America, Europe (Flament et al., 2008; Conway et al., 2019) and Japan (Kurisu et al., 2016). These studies
105 suggest that anthropogenic Fe signatures originating from metallurgical, industrial and urban activities can
106 display significant differences in Fe isotopes relative to natural sources. However, the understanding of
107 the potential fractionation of Fe in ore smelting/refining remains unclear. Only one study has been
108 conducted to date, which examines Fe production by an ancient Galo-Roman bloomery process. The study
109 of a major Roman site of Fe production known as “Les Martyrs” (Montagne Noire Massif, SW France)
110 showed no significant Fe isotope fractionation from the Roman production of iron bars (Milot et al.,
111 2016). Thus, the present study aims to explore (1) the Fe isotope fractionation associated with Ni-rich
112 laterite ore formation, (2) the Fe isotope fractionation associated with Ni laterite ore smelting and refining
113 during the RKEF processing, and (3) the potential of Fe isotopes to trace the environmental impact of
114 FeNi production.

115 **2. Materials and methods**

116 **2.1. Ore deposit and mining contexts**

117 The RKEF process for the production of FeNi was first developed in 1953-1954 and was applied
118 commercially to the treatment of garnieritic ores in New Caledonia. Later, it was adopted by FeNi
119 producers for Ni ore deposits across the globe: the Dominican Republic, Colombia, Venezuela, Indonesia,
120 Japan, etc. (Warner et al., 2006). In recent years, at least three major new FeNi smelters have been
121 constructed and are in operation: Barro Alto and Onça Puma in Brazil and Koniambo in New Caledonia
122 (Oxley et al., 2016). The Ni deposits of Barro Alto, located in the midwestern region of Goiás (in Central
123 Brazil), constitute a large Ni reserve that is exploited by the Anglo American company using open pits.

124 The metallurgical plant at Barro Alto uses the RKEF process to produce FeNi from a nominal 2.4
125 Mt/y of ore. Its production has increased nearly 2-fold since 2011 to 43 kt of total Ni output in 2018
126 (Anglo American PLC Annual Report, 2012 and 2018). The deposit, with the ore reserves estimated in
127 2018 at 52 Mt containing 586 kt of Ni (Anglo American PLC Annual Report, 2018), is in the Barro Alto
128 mafic-ultramafic complex that is part of the Pre-Cambrian shield. This ultramafic complex is composed of
129 serpentized dunites, pyroxenites and gabbros (Ferreira Filho et al., 2010). The mineralization
130 corresponds to the weathered surficial portions of the serpentinites (Butt and Cluzel, 2013).

131 Four main steps are involved in FeNi production (Crundwell et al., 2011): drying of the ore before
132 its introduction into the rotating kiln; calcination with coal, oil or other organic products within the kiln;
133 reduction in an electric furnace and refining of the molten FeNi in another electric furnace (Fig. 1). These
134 processes generate enormous quantities of by-products (Dalvi et al., 2004; Warner et al., 2006) containing
135 significant amounts of metals (e.g., Ni, Co, Cr, Mn, Fe) (Ettler et al., 2016).

136 The fly ash (F) generated contains large amounts of Fe and Ni and is recovered by electrostatic
137 filters. The collected fly ash is then recycled into the calcination kiln (Fig. 1). The smelting slags (SS) are
138 composed of high temperature silicates, amorphous glass as well as inclusions of small FeNi metallic
139 particles (Ettler et al., 2016). They are dumped and stored near the plant. The molten FeNi is then refined
140 through a two-step process that produces two types of refining slags: black refining slag (BRS) and white
141 refining slag (WRS) after the removal of P and S, respectively. The FeNi is produced in the form of small
142 ingots or water-granulated “beans”.

143 **2.2. Samples**

144 The list of samples is detailed in Table 1. The sampling for Fe isotope determinations included
145 geogenic samples from soils and lateritic profiles in the Barro Alto ultramafic region (8 samples) and
146 materials used and produced during the RKEF processes (7 samples). The samples were selected based on
147 previous studies performed by our team on the Barro Alto massif (Ratié et al., 2015, 2016, 2018). The
148 choice was closely related to (i) the largest Fe concentration variations to seek hypothetical isotopic

149 fractionation associated with Fe enrichment, Fe-bearing phases and Fe oxidation state changes along
150 different sections in the lateritic profile and (ii) the most significant Ni isotope variations used to decipher
151 different chemical mechanisms involved in lateritization and smelting processes.

152 The anthropogenic materials included the Ni ores employed as feeding material (n=2), the
153 smelting slags (SS, n=2), white and black refining slags (WRS and BRS, n=2) and the final manufactured
154 FeNi ingot (n=1). As previously mentioned, the fly ash is reinjected in the calcination step.

155 A 28 m deep lateritic profile drilled by the Anglo American company, sampled at intervals of 1 m,
156 labeled "RC", was used for this study (Ratié et al., 2018). As the overburden (0-3 m) was removed to
157 facilitate drilling by the mining company, the core/profile starts at a depth of 3 m. To complete the profile,
158 soil in the vicinity was collected at three different depths: 0-10 cm (BAS1 0-10) or topsoil, 10-30 cm
159 (BAS1 10-30) and 30-80 cm (BAS1 30-80) (Ratié et al., 2015). Five lateritic samples of the RC profile
160 (RC0-1, RC6-7, RC16-17, RC24-25, and RC27-28) were selected for Fe isotope characterization. RC0-1
161 was defined as the top of the lateritic profile. RC6-7 was the part of the lateritic profile dominated by Fe
162 oxides. RC16-17 was the smectitic horizon exhibiting high Ni content, and RC24-25 was a characteristic
163 saprolitic sample rich in serpentine and exhibiting a relatively low Fe content. RC27-28 was the deepest
164 sample, mainly composed of primary minerals (olivine) and was considered the protolith. The sample
165 selection strategy involved the sampling of a weathering gradient of the ultramafic parent rock.

166 **2.3. Sample preparation and Fe chemical separation**

167 All the samples were homogenized and finely crushed, and approximately 100 mg of the samples
168 was aliquoted to Savillex vessels. The samples were then digested on a hot plate using a multiple-step acid
169 procedure with HF, HNO₃, and HCl. First, an acid mixture of 5 mL of concentrated HF and 1.5 mL of
170 HClO₄ at 180°C was added until evaporation was complete. Subsequently, a mixture of concentrated HCl-
171 HNO₃ (3.75 mL and 1.25 mL, respectively) at 150°C was added and evaporated to dryness. Finally, the
172 samples were dissolved in an acid medium of 6 M HCl and split into aliquots for elemental and isotopic
173 determinations. For this step, the sample solution aliquots were processed through chromatographic

174 columns for chemical separation prior to isotope analysis. The iron was purified using Bio Rad AG1 X4
 175 (200–400 mesh) anionic resin loaded into thermo-retractable Teflon columns for exchange
 176 chromatography in an HCl medium as described by Poitrasson et al. (2004). Blank levels of the chemical
 177 procedure reached ~4 ng of Fe, which is negligible for the sample preparation process. All of the reagents
 178 were of analytical grade or bidistilled and the sample preparation for isotope analysis was conducted in the
 179 clean laboratories of GEOPS (Université Paris Saclay, France).

180 **2.4. Iron isotope composition measurements**

181 Iron isotope measurements were performed at the GET laboratory (Toulouse, France) using the
 182 Observatoire Midi-Pyrénées ICP facility in high or medium mass resolution mode on a Thermo Electron
 183 Neptune MC ICP MS. The Fe isotopic ratios were determined following the procedure detailed by
 184 Poitrasson and Freydier (2005).

185 This method involved a mass bias correction using a combination of the “standard-sample
 186 bracketing” approach using IRMM-14 as the Fe standard and Ni doping of the purified Fe samples. This
 187 approach accurately corrected for mass bias deviations due to residual matrix effects. The Fe isotope
 188 compositions were expressed in the delta notation relative to the European reference material IRMM-14 as
 189 follows:

$$190 \quad \delta^{57}Fe = \left(\frac{\left(\frac{{}^{57}Fe}{{}^{54}Fe} \right)_{sample}}{\left(\frac{{}^{57}Fe}{{}^{54}Fe} \right)_{IRMM-14}} - 1 \right) \times 1000 \text{ (Eq. 1).}$$

191 The GET in-house hematite standard from Milhas (Pyrénées, France) was measured every 6
 192 samples. The long-term external reproducibility of the method was estimated from replicate analyses of
 193 this standard in every session. In this work, the mean $\delta^{57}Fe$ value of individual measurements for hematite
 194 was 0.762 ± 0.083 ‰ (2 SD, n=21) in the GET laboratory, whereas data pooled in groups of 3 (which is
 195 the minimum number of times each sample should normally be analyzed) yielded a $\delta^{57}Fe = 0.764 \pm 0.057$
 196 ‰ (2 SD, n=7). These values are consistent with those from previous measurements conducted for over

197 three years in the same analytical sequences and performed in various laboratories (Poitrasson et al.,
 198 2014). Variation in the $\delta^{57}\text{Fe}$ reported for the samples in this study is expressed as two standard errors (2
 199 SE) of the mean (n=3).

200 **3. Results and discussion**

201 **3.1. Bulk compositions**

202 The mineralogy and chemical composition of the entire set of samples are discussed in detail in
 203 Ratié et al. (2015, 2016) and Ettlér et al. (2016). The weathered material derived from the ultramafic rocks
 204 is strongly depleted in Mg and enriched in Fe from the base to the top of the weathering profile. The
 205 mineralogy of the weathered profile changes from the base (RC27-28) to the top (BAS1 0-10, BAS1 10-
 206 30, BAS1 30-80) from the dominance of primary minerals (serpentine, chlorite, amphibole, olivine and
 207 traces of quartz) to secondary minerals such as goethite and hematite with some preserved primary
 208 minerals such as chromite. Moreover, in order to quantify the geochemical changes in laterite developed
 209 above ultramafic rocks, the ultramafic index of alteration (UMIA) was calculated using molar ratios
 210 (Babechuk et al., 2014; Aiglsperger et al., 2016), Eq 2:

$$UMIA = 100 \times \left[\frac{Al_2O_3 + Fe_2O_3}{SiO_2 + MgO + Al_2O_3 + Fe_2O_3} \right] \quad (Eq. 2)$$

211 Furthermore, a ternary plot illustrates the general weathering trend of UM weathering in Barro
 212 Alto (Fig. 2) with the initial loss of MgO, followed by SiO₂ losses and concomitant enrichment of Al₂O₃
 213 and especially Fe₂O₃ (Fig. 2). However, the strong secondary silicification (chalcedony) in the lateritic
 214 regolith in Barro Alto modified the trend of the SiO₂ losses (Ratié et al., 2018) and explained the relatively
 215 low UMIA values. This study's unweathered material has a UMIA value of 4% whereas other lateritic
 216 samples from the profile exhibit UMIA values ranging from 6 to 44% (Table 1). Soil samples present
 217 homogeneous UMIA values from 34 to 39%.

218 Based on the overall sampling from Ratié et al. (2016), the industrial plant feeding material, i.e.,
 219 the ore, exhibits high Fe and Mg contents of 118-178 g kg⁻¹ and 81.4-110 g kg⁻¹, respectively, whereas Ni

220 content ranges from 16.9 to 23.2 g kg⁻¹. Iron and Mg contents of the smelting slags (SS) range from 68.8
221 to 142.7 g kg⁻¹ and 153 to 188 g kg⁻¹, respectively, and the Ni concentration is relatively low (≤ 2 g kg⁻¹).

222 According to a previous study of these smelting wastes (Ettler et al., 2016), more than 95% of the
223 total Fe occurs as Fe(II) in the smelting slag, whereas 80% of the total Fe in the reinjected fly ash is
224 present as Fe(III). The refined slags (WRS and BRS) are richer in Fe (71.2-179 g kg⁻¹) compared with
225 smelting slags. Ferronickel is composed of roughly two-thirds Fe (66-69 wt%) and one-third Ni (31-34
226 wt%).

227 The Anglo American plant uses 2.4 Mt/y of Ni ore to produce 41,000 t/y of Ni as FeNi (Moore,
228 2012 and personal communications). The quantity of Ni introduced in the process, as calculated using an
229 ore Ni content of 1.96 ± 0.23 wt%, is $47,000 \pm 5,400$ t/y. This led to a production yield of nearly $88 \pm 10\%$
230 Ni for the 2016 production (Anglo American PLC Annual Report, 2017). For Fe, given the mean Fe
231 content in ore of 15.1 wt% and a production of 41,000 t of FeNi, 362,400 t of Fe were processed and
232 82,000 t of Fe were produced as FeNi with almost 80% of the initial Fe remaining in the waste. The
233 difference between the incoming Fe/Ni and FeNi production corresponds to the residual Fe/Ni in the
234 different waste materials.

235 **3.2. Iron isotope compositions**

236 **3.2.1. Ultramafic rocks weathering**

237 Based on mantle-derived and crustal igneous rocks, the bulk silicate Earth shows a homogenous
238 Fe isotopic signature of approximately $\delta^{57}\text{Fe} = 0.10 \pm 0.03\%$ (Poitrasson and Freydier, 2005; Poitrasson,
239 2006; Johnson and Beard, 2006). In Barro Alto, the deepest sample from the profile (RC27-28), which
240 contains the typical mineral assembly of serpentinized ultramafic rocks, was determined to be the least
241 weathered sample and thus, it was considered representative of the protolith material (Ratié et al., 2018).
242 The base of the weathering profile ($0.08 \pm 0.20\%$) is consistent with the bulk silicate Earth value
243 (Poitrasson, 2006).

244 The $\delta^{57}\text{Fe}$ values of the weathered materials range from $-0.10 \pm 0.07\text{‰}$ (BAS1 0-10) to $0.07 \pm$
245 0.05‰ (RC0-1) and fall within the range of values reported in the literature for soils (Wu et al., 2019).
246 Given the level of analytical variation (2 SE), these results show no significant isotopic differences in
247 $\delta^{57}\text{Fe}$ values between the protolith and the weathered materials, similarly to other lateritic profiles
248 elsewhere. (Cameroon, Poitrasson et al., 2008) (China, Liu et al., 2014; Philippines, Li et al., 2017).
249 Therefore, Fe isotope composition remains constant during the UM weathering in the Barro Alto complex.
250 In contrast, in Ni's case, weathering was associated with isotopic fractionation as part of the Ni was
251 leached, leading to a weathering profile depleted in heavy Ni isotopes. This depletion of heavy Ni isotopes
252 was interpreted as the preferential sorption and incorporation of light Ni isotopes into Fe oxides
253 (Wasylenki et al., 2015) and phyllosilicates (type 2:1) (Ratié et al., 2018) in addition to Ni isotopic
254 fractionation during the first stage of weathering, i.e., during mineral dissolution (Ratié et al., 2015, 2018).

255 Moreover, the gain and loss of Fe during chemical weathering can be evaluated by calculating the
256 enrichment factor " τ_{Fe} " (Table 1). A negative value for τ_{Fe} reflects a true loss in Fe from the weathered
257 material compared with the protolith, and a positive value indicates a gain in Fe. If τ_{Fe} is 0, Fe is
258 considered immobile during weathering with respect to the regolith. The entire Barro Alto profile displays
259 τ_{Fe} values ranging from -0.10 to 0.22, which suggests that Fe shows little mobility from all of the profile
260 layers (Table 1, Fig. 3). However, a caveat is that this inference does not consider possible soil density
261 changes that were not measured in this study. The topography of the complex is characterized by a
262 succession of hills and valleys with altitudes ranging from 750 m to 1100 m dominating the large plain
263 (De Oliveira et al., 1992). As a consequence, the weathering conditions occurring on the complex are
264 considered as well drained. Under tropical conditions, from base to top of the profile, olivine and
265 serpentine are replaced by Fe-oxides and Mg silicates through a series of transitional phyllosilicates (Colin
266 et al. 1990; Butt and Cluzel, 2013). In addition, bulk Fe isotopic compositions remain homogeneous along
267 the lateritic profile (-0.10‰ to 0.08‰), indicating that $\delta^{57}\text{Fe}$ values were not significantly altered by Fe
268 loss or gain during chemical weathering (Fig 3). These features agree with the oxidative conditions along

269 the lateritic profile and the high rate of lixiviation. Therefore, the formation of secondary Fe-bearing
270 phases plays a minor role in fractionating Fe isotope during ultramafic rock weathering.

271 Additionally, even with the relatively high uncertainty on the least weathered sample (RC27-28),
272 lateritic profile resulting from peridotites weathering (Li et al., 2017; our study) displayed a $\delta^{57}\text{Fe}$ lighter
273 than those resulting from crustal rocks weathering (basalt: Liu et al., 2014, granodioritic rock: Poitrasson
274 et al., 2008). This feature may be explained by the lighter mean $\delta^{57}\text{Fe}$ of peridotites relative to Earth's
275 crustal rocks (Weyer and Ionov, 2007; Zhao et al., 2010; Craddock et al., 2013; Poitrasson et al., 2013).

276 3.2.2. Metallurgical production

277 The Fe isotopic composition of the metallurgical samples ranges from $-0.10 \pm 0.09\text{‰}$ (smelting
278 slags) to $0.07 \pm 0.12\text{‰}$ (FeNi). The Fe isotope compositions are analytically indistinguishable from the
279 feeding materials to the final FeNi product, in contrast to Ni isotopes (Fig. 4).

280 Although the process yields for Fe are very low (22%), the isotope composition is homogeneous
281 in all by-products. Given the high-temperature natural processes that occur in the Earth's core and the
282 differentiation in an early silicate magma ocean, it seems logical that there is not significant Fe isotope
283 fractionation in the FeNi alloy and the ultramafic silicate melt (Poitrasson et al., 2009). Within the 2-7.7
284 GPa pressures, the chemical and Fe isotope equilibrium was reached at 2,000°C within 100 s ($\Delta^{57}\text{Fe}_{\text{metal-}}$
285 $\text{silicate glass} = 0.047 \pm 0.063 \text{‰}$). The high temperature conditions found in the electric furnace at 1,600°C
286 could induce a similar rapid equilibrium and hence inhibit detectable Fe isotopic fractionation between
287 FeNi and the feeding material.

288 In the furnace, metal isotope fractionation is dependent on the relative isotope mass difference, the
289 viscosity of the alloy, the mass of the matrix atoms and the temperature range (Ott, 1969; Lodding et al.,
290 1970; Ginoza and March, 1985). In the RKEF processes, the smelting temperature (1,600°C) is very close
291 to the Fe fusion point (1,538°C), and the homogeneous $\delta^{57}\text{Fe}$ value in the metallurgical wastes argues for
292 an absence of the thermal gradients responsible for possible metal stable isotope fractionation. In fact, in
293 modern enhanced industrial processes such as RKEF, the Fe distribution is homogeneous at the molten

294 scale during the different steps. This inference is supported by experiments reproducing the ancient
295 bloomery process at 1,300°C, which shows no significant Fe isotopic heterogeneity within the Fe metal
296 products, although they did not go beyond the pasty state at such low temperatures (Milot et al., 2016).

297 **3.2.3. Implications for environmental tracing**

298 Our results demonstrated no evidence of significant Fe isotope fractionation in the whole
299 sequence of lateritization and the smelting activities in Barro Alto, leading to conservation of the Fe
300 isotopic signature. This result implies that Fe is a conservative isotope tracer for Fe-ores and metals
301 limonitic ores. Therefore, the mean $\delta^{57}\text{Fe}$ value was set at 0.01 ± 0.11 ‰ (2SD) for the whole samples
302 (lateritic, soil, slags, and FeNi) from the Barro Alto UM complex (Fig. 5).

303 Such an outcome hinders the use of Fe isotopes as an environmental tracer in the context of soils
304 impacted by metallurgical activity if the raw material comes from the same locality, which is the case at
305 Barro Alto. However, the conservation of the $\delta^{57}\text{Fe}$ values from the feeding material to the metallurgical
306 wastes can be advantageous to trace anthropogenic sources in cases (i) where pyrometallurgical plants use
307 feeding material imported from another deposit exhibiting $\delta^{57}\text{Fe}$ values that are distinct from local
308 environment and when (ii) the metallurgical by-products deposited in open-air undergo redox reactions
309 triggered by changes in the biogeochemical conditions of the surrounding environment. A compilation of
310 published $\delta^{57}\text{Fe}$ of ores (Milot et al., 2016, 2018) has noted that the iron isotopic signature exhibits a wide
311 range of values from -2.8 ‰ to 2.4 ‰ for different mineral deposits (sedimentary, hydrothermal, skarn
312 and supergene deposits (e.g., Graham et al., 2004; Markl et al., 2006; Johnson et al., 2008; Fabre et al.,
313 2011; Wang et al., 2011; Cheng et al., 2015; Pi et al., 2015; Wawryk and Foden, 2015; Texeira et al.,
314 2017). Moreover, modern soils from temperate areas (e.g., Fantle and Depaolo, 2004; Emmanuel et al.,
315 2005; Wiederhold et al., 2007; Fekiacova et al., 2013, Wu et al., 2019) and wet tropical soils involving Fe
316 redox cycling (Thompson et al., 2007; Akerman et al., 2014) yield $\delta^{57}\text{Fe}$ ranges of -0.78 ‰ to 1.08 ‰ (Wu
317 et al., 2019). This range represents significant variations relative to the natural $\delta^{57}\text{Fe}$ values in Barro Alto
318 soils, ranging from -0.10 ‰ to 0.02 ‰ only. Based on the Fe isotopic range of the non-UM soils, we

319 performed a calculation to estimate the amount of smelting slags needed to create a significant shift in the
320 non-UM soils (Supplementary Information). That permits the use of Fe isotopes to trace contamination
321 when raw materials from other locations are employed, as long as they are not regular lateritic soils.
322 Therefore, the use of a different feeding material for the industrial plant at the Barro Alto site would allow
323 tracing of the anthropogenic input to the local environment. In this case, Fe isotopes could be a better
324 tracer than Ni isotopes that showed isotope fractionation during the smelting process (Ratié et al., 2016)
325 and a much larger range of isotopic composition in the soil and lateritic ores (Fig. 4).

326 Finally, a review published by Warner et al. (2006) has shown similar concentration results during
327 different steps of the Ni RKEF smelting processes throughout the world (the Dominican Republic,
328 Colombia, Venezuela, Brazil, Japan, New Caledonia, Indonesia, Ukraine, Macedonia and Greece). The
329 feeding material from Barro Alto exhibits means concentration values of 2 wt% of Ni and 15.3 wt% of Fe
330 ($n = 13$, Ratié et al., 2016), whereas the global average is 1.9 ± 0.5 wt% and 17 ± 5 wt%, respectively. The
331 total average Fe content in slag material is 10 wt% at Barro Alto, whereas the global mean value is $15 \pm$
332 10 wt%. The feeding material composition and the main wastes are, therefore, similar for the Barro Alto
333 smelter and the global laterite Ni smelters. Moreover, the calcination, smelting and refining temperatures
334 used are similar for the Barro Alto plant (850°C, 1,600°C and 1,550°C, respectively) and the other cited
335 RKEF smelters ($880 \pm 120^\circ\text{C}$, $n=13$; $1,570 \pm 35^\circ\text{C}$, $n = 12$; $1,440 \pm 120^\circ\text{C}$, $n = 10$, respectively). This
336 comparison suggests that the Fe isotope system's behavior during pyrometallurgical processing at the
337 Barro Alto plant is likely applicable to other plants elsewhere in the world.

338 4. Conclusions

339 For the first time, this study shows the Fe isotope composition for the complete series of natural
340 and anthropogenic processes in the Barro Alto ultramafic complex. No significant Fe isotope variations
341 were identified in either the pedogenesis of lateritic soils or the pyrometallurgical processes of Ni ore
342 refining. The $\delta^{57}\text{Fe}$ value of the protolith fell within the range of the Fe isotope composition of the bulk
343 silicate Earth, which is estimated at approximately 0.1 ‰ (Poitrasson, 2006), and is similar to deep

344 lateritic profiles studied elsewhere. In the Ni laterite RKEF smelting process at Barro Alto, the rapid
345 equilibrium of Fe isotopes between the different phases composing the FeNi ore melt at 1,600°C in the
346 electric furnace results in undetectable Fe isotopic fractionation. Laboratory experiments support this
347 mechanism under controlled conditions with high pressure and temperature equilibration between FeNi
348 alloys and ultramafic silicate melts (Poitrasson et al., 2009).

349 As a consequence, the $\delta^{57}\text{Fe}$ values obtained from both pedogenesis (protolith to topsoil) and
350 pyrometallurgical samples are homogeneous and may challenge the discrimination of anthropic and
351 natural sources. Further studies should verify the potential fractionation induced by postdepositional
352 processes as demonstrated for Ni (Ratié et al., 2016) and Zn (Yin et al., 2018). Nonetheless, the
353 conservation of the $\delta^{57}\text{Fe}$ values from the ores to the by-products is an advantage for tracing
354 anthropogenic sources when (i) the pyrometallurgical plant uses feeding material with Fe ores imported
355 from other geological unities exhibiting different $\delta^{57}\text{Fe}$ values and/or (ii) the by-products are transported
356 or dispersed to other locations with different $\delta^{57}\text{Fe}$ values in the topsoil. In these cases, Fe isotopes could
357 be a more suitable environmental tracer of anthropogenic sources than Ni isotopes for tracing
358 contamination in non-UM soils related to mining and smelting materials dispersion.

359 **Acknowledgments**

360 We express our sincere thanks to the Anglo American staff at the Barro Alto mine (Goiás, Brazil).
361 The authors acknowledge Gael Monvoisin for maintaining the GEOPS clean laboratory facilities and J.
362 Chmeleff from the GET laboratory (Toulouse, France) for maintaining the MC ICP MS in good working
363 order. The analytical work in Toulouse along with travel by JG and LCV was partly funded by the LMI-
364 OCE and the 7th European Community Framework Program (NIDYFICS, n°318123) and the CLIM-
365 AMAZON laboratory (INCO-LAB grant n°295091). The analytical work in Brazil and France was partly
366 funded by the LMI-OCE and CNPq 445423/2014-5, 400029/2015-4 and 420697/2018-7. Gildas
367 acknowledges the Faculty of Environmental Sciences, Czech University of Life Sciences, Prague (Grant

368 n° 42900/1312/3166), the Czech Science Foundation 18-07585S, the French Ministry of National
 369 Education and Research (G. Ratié PhD grant), CAPES and the CNPq for support during his PhD. Jérémie
 370 Garnier was supported by CNPq grant 302722/2018-1. Daniel F. Araújo thanks the POLLUSOLS project
 371 framework and IFREMER (Centre Atlantique) for the financial support.

372 **References**

- 373 Aiglsperger, T., Proenza, J.A., Lewis, J.F., Labrador, M., Svojtka, M., Rojas-Puron, A., Longo, F.,
 374 Ďurišová, J., 2016. Critical metals (REE, Sc, PGE) in Ni laterites from Cuba and the
 375 Dominican Republic. *Ore Geology Reviews* 73, 127–147.
- 376 Anglo American PLC Annual Report, 2012, 2012.
- 377 Anglo American PLC Annual Report, 2017, 2017.
- 378 Anglo American PLC Annual Report, 2018, 2018.
- 379 Akerman, A., Poitrasson, F., Oliva, P., Audry, S., Prunier, J., Braun, J.J., 2014. Isotopic fingerprint of Fe
 380 cycling in an equatorial soil-plant-water system: The Nsimi watershed, South Cameroon.
 381 *Chemical Geology*, 385: 104-116.
- 382 Araújo, D.F., Ponzevera, E., Briant, N., Knoery, J., Sireau, T., Mojtahid, M., Metzger, E., Brach-Papa, C.,
 383 2019a. Assessment of the metal contamination evolution in the Loire estuary using Cu and Zn
 384 stable isotopes and geochemical data in sediments. *Mar. Pollut. Bull.* 143, 12–23.
- 385 Araújo, D. F., Ponzevera, E., Briant, N., Knoery, J., Bruzac, S., Sireau, T., Brach-Papa, C., 2019b. Copper,
 386 zinc and lead isotope signatures of sediments from a mediterranean coastal bay impacted by
 387 naval activities and urban sources. *Applied Geochemistry*, 111, 104440.
- 388 Babechuk, M.G., Widdowson, M., Kamber, B.S., 2014. Quantifying chemical weathering intensity and
 389 trace element release from two contrasting basalt profiles, Deccan Traps, India. *Chemical*
 390 *Geology* 363, 56–75.
- 391 Barna, R., Moszkowicz, P., Gervais, C., 2004. Leaching assessment of road materials containing primary
 392 lead and zinc slags. *Waste Manag.* 24, 945–955.
- 393 Beard, B.L., Handler, R.M., Scherer, M.M., Wu, L., Czaja, A.D., Heimann, A., Johnson, C.M., 2010. Iron
 394 isotope fractionation between aqueous ferrous iron and goethite. *Earth Planet. Sci. Lett.* 295,
 395 241–250.
- 396 Bigalke, M., Weyer, S., Kobza, J., & Wilcke, W., 2010. Stable Cu and Zn isotope ratios as tracers of
 397 sources and transport of Cu and Zn in contaminated soil. *Geochimica et Cosmochimica*
 398 *Acta*, 74(23), 6801-6813.
- 399 Borrok, D.M., Wanty, R.B., Ridley, W.I., Lamothe, P.J., Kimball, B.A., Verplanck, P.L., Runkel, R.L.,
 400 2009. Application of iron and zinc isotopes to track the sources and mechanisms of metal
 401 loading in a mountain watershed. *Appl. Geochem.* 24, 1270–1277.
 402 <https://doi.org/10.1016/j.apgeochem.2009.03.010>
- 403 Bril, H., Zainoun, K., Puziewicz, J., Courtin-Nomade, A., Vanaecker, M., Bollinger, J.-C., 2008.
 404 Secondary phases from the alteration of a pile of zinc-smelting slag as indicators of

- 405 environmental conditions: An example from Swietochłowice, Upper Silesia, Poland. *Can.*
406 *Mineral.* 46, 1235–1248.
- 407 Bullen, T.D., 2014. 7.10 - Metal Stable Isotopes in Weathering and Hydrology, in: Holland, H.D.,
408 Turekian, K.K. (Eds.), *Treatise on Geochemistry (Second Edition)*. Elsevier, Oxford, pp. 329–
409 359.
- 410 Butt, C.R., Cluzel, D., 2013. Nickel laterite ore deposits: weathered serpentinites. *Elements* 9, 123–128.
- 411 Chen, J. B., Busigny, V., Gaillardet, J., Louvat, P., & Wang, Y. N. (2014). Iron isotopes in the Seine River
412 (France): Natural versus anthropogenic sources. *Geochimica et Cosmochimica Acta*, 128, 128–
413 143.
- 414 Cheng, Y.B., Mao, J.W., Zhu, X.K., Wang, Y., 2015. Iron isotope fractionation during supergene
415 weathering process and its application to constrain ore genesis in Gaosong deposit, Gejiu
416 district, SW China. *Gondwana Research*, 27(3): 1283-1291.
- 417 Chrastný, V., Čadková, E., Vaněk, A., Teper, L., Cabala, J., Komárek, M., 2015. Cadmium isotope
418 fractionation within the soil profile complicates source identification in relation to Pb–Zn
419 mining and smelting processes. *Chem. Geol.* 405, 1–9.
420 <https://doi.org/10.1016/j.chemgeo.2015.04.002>
- 421 Colin, F., Nahon, D., Trescases, J. J., & Melfi, A. J. (1990). Lateritic weathering of pyroxenites at
422 Niquelandia, Goiás, Brazil; the supergene behavior of nickel. *Economic Geology*, 85(5), 1010–
423 1023.
- 424 Conway, T.M., Hamilton, D.S., Shelley, R.U., Aguilar-Islas, A.M., Landing, W.M., Mahowald, N.M.,
425 John, S.G., 2019. Tracing and constraining anthropogenic aerosol iron fluxes to the North
426 Atlantic Ocean using iron isotopes. *Nat. Commun.* 10, 1–10.
- 427 Craddock, P.R., Warren, J.M., Dauphas, N., 2013. Abyssal peridotites reveal the near-chondritic Fe
428 isotopic composition of the Earth. *Earth and Planetary Science Letters* 365, 63–76.
- 429 Crundwell, F.K., Moats, M.S., Ramachandran, V., Robinson, T.G., Davenport, W.G., 2011. Chapter 7 -
430 Refining Molten Ferronickel, in: Davenport, F.K.C.S.M.R.G.R.G. (Ed.), *Extractive Metallurgy*
431 *of Nickel, Cobalt and Platinum Group Metals*. Elsevier, Oxford, pp. 85–93.
- 432 Dalvi, A.D., Bacon, W.G., Osborne, R.C., 2004. Past and future of nickel laterite projects.
- 433 Dauphas, N., John, S.G., Rouxel, O., 2017. Iron isotope systematics. *Rev. Mineral. Geochem.* 82, 415–
434 510.
- 435 De Oliveira, S. B., Trescases, J. J., & Melfi, A. J. (1992). Lateritic nickel deposits of Brazil. *Mineralium*
436 *deposita*, 27(2), 137-146.
- 437 Dublet, G., Juillot, F., Morin, G., Fritsch, E., Fandeur, D., Brown, G.E., 2015. Goethite aging explains Ni
438 depletion in upper units of ultramafic lateritic ores from New Caledonia. *Geochim.*
439 *Cosmochim. Acta* 160, 1–15. <https://doi.org/10.1016/j.gca.2015.03.015>
- 440 Dublet, G., Juillot, F., Morin, G., Fritsch, E., Fandeur, D., Ona-Nguema, G., Brown, G.E., 2012. Ni
441 speciation in a New Caledonian lateritic regolith: A quantitative X-ray absorption spectroscopy
442 investigation. *Geochim. Cosmochim. Acta* 95, 119–133.
- 443 Emmanuel, S., Erel, Y., Matthews, A., Teutsch, N., 2005. A preliminary mixing model for Fe isotopes in
444 soils. *Chem. Geol.* 222, 23–34.
- 445 Ettler, V., Johan, Z., 2014. 12 years of leaching of contaminants from Pb smelter slags:
446 Geochemical/mineralogical controls and slag recycling potential. *Appl. Geochem.* 40, 97–103.

- 447 Ettler, V., Kvapil, J., Šebek, O., Johan, Z., Mihaljevič, M., Ratié, G., Garnier, J., Quantin, C., 2016.
448 Leaching behaviour of slag and fly ash from laterite nickel ore smelting (Niquelândia, Brazil).
449 *Appl. Geochem.* 64, 118–127.
- 450 Ettler, V., Polák, L., Mihaljevič, M., Ratié, G., Garnier, J., Quantin, C., 2018. Oral bioaccessibility of
451 inorganic contaminants in waste dusts generated by laterite Ni ore smelting. *Environ.*
452 *Geochem. Health* 40, 1699–1712.
- 453 Fabre, S., Nedelec, A., Poitrasson, F., Strauss, H., Thomazo, C., Nogueira, A., 2011. Iron and sulphur
454 isotopes from the Carajas mining province (Para, Brazil): Implications for the oxidation of the
455 ocean and the atmosphere across the Archaean-Proterozoic transition. *Chemical Geology*,
456 289(1-2): 124-139.
- 457 Fantle, M.S., DePaolo, D.J., 2004. Iron isotopic fractionation during continental weathering. *Earth Planet.*
458 *Sci. Lett.* 228, 547–562.
- 459 Fekiacova, Z., Pichat, S., Cornu, S., Balesdent, J., 2013. Inferences from the vertical distribution of Fe
460 isotopic compositions on pedogenetic processes in soils. *Geoderma*, 209: 110-118.
- 461 Ferreira Filho, C.F., Pimentel, M.M., de Araujo, S.M., Laux, J.H., 2010. Layered intrusions and volcanic
462 sequences in Central Brazil: geological and geochronological constraints for Mesoproterozoic
463 (1.25 Ga) and Neoproterozoic (0.79 Ga) igneous associations. *Precambrian Res.* 183, 617–634.
- 464 Flament, P., Mattielli, N., Aimoz, L., Choel, M., Deboudt, K., de Jong, J., Rimetz-Planchon, J., Weis, D.,
465 2008. Iron isotopic fractionation in industrial emissions and urban aerosols. *Chemosphere* 73,
466 1793–1798. <https://doi.org/10.1016/j.chemosphere.2008.08.042>
- 467 Gall, L., Williams, H.M., Halliday, A.N., Kerr, A.C., 2017. Nickel isotopic composition of the mantle.
468 *Geochim. Cosmochim. Acta* 199, 196–209. <https://doi.org/10.1016/j.gca.2016.11.016>
- 469 Ganne, P., Cappuyns, V., Vervoort, A., Buvé, L., Swennen, R., 2006. Leachability of heavy metals and
470 arsenic from slags of metal extraction industry at Angleur (eastern Belgium). *Sci. Total*
471 *Environ.* 356, 69–85. <https://doi.org/10.1016/j.scitotenv.2005.03.022>
- 472 Ginoza, M., March, N.H., 1985. Isotope Effects in Liquid Metals. *Phys. Chem. Liq.* 15, 75–111.
473 <https://doi.org/10.1080/00319108508078471>
- 474 Graham, S., Pearson, N., Jackson, S., Griffin, W., O'Reilly, S.Y., 2004. Tracing Cu and Fe from source to
475 porphyry: in situ determination of Cu and Fe isotope ratios in sulfides from the Gratsberg Cu-
476 Au deposit. *Chemical Geology*, 207: 147-169.
- 477 Herbert Jr, R.B., Schippers, A., 2008. Iron isotope fractionation by biogeochemical processes in mine
478 tailings. *Environ. Sci. Technol.* 42, 1117–1122.
- 479 Houben, D., Couder, E., Sonnet, P., 2013. Leachability of cadmium, lead, and zinc in a long-term
480 spontaneously revegetated slag heap: implications for phytostabilization. *J. Soils Sediments* 13,
481 543–554.
- 482 Johnson, C.M., Beard, B.L., 2006. Fe isotopes: an emerging technique for understanding modern and
483 ancient biogeochemical cycles. *GSA TODAY* 16, 4.
- 484 Johnson, C. M., Beard, B. L., & Roden, E. E., 2008. The iron isotope fingerprints of redox and
485 biogeochemical cycling in modern and ancient Earth. *Annu. Rev. Earth Planet. Sci.*, 36, 457-
486 493.
- 487 Kavner, A., John, S.G., Sass, S., Boyle, E.A., 2008. Redox-driven stable isotope fractionation in transition
488 metals: Application to Zn electroplating. *Geochim. Cosmochim. Acta* 72, 1731–1741.
- 489 Klein, S., & Rose, T. (2020). Evaluating copper isotope fractionation in the metallurgical operational

- 490 chain: An experimental approach. *Archaeometry*.
- 491 Kurisu, M., Takahashi, Y., Iizuka, T., Uematsu, M., 2016. Very low isotope ratio of iron in fine aerosols
492 related to its contribution to the surface ocean. *J. Geophys. Res. Atmospheres* 121, 11,119-
493 11,136.
- 494 Li, M., He, Y.S., Kang, J.T., Yang, X.Y., He, Z.W., Yu, H.M., Huang, F., 2017. Why was iron lost
495 without significant isotope fractionation during the lateritic process in tropical environments?
496 *Geoderma*, 290: 1-9.
- 497 Liu, S.A., Teng, F.Z., Li, S.G., Wei, G.J., Ma, J.L., Li, D.D., 2014. Copper and iron isotope fractionation
498 during weathering and pedogenesis: Insights from saprolite profiles. *Geochimica Et*
499 *Cosmochimica Acta*, 146: 59-75.
- 500 Lodding, A., Mundy, J.N., Ott, A., 1970. Isotope Inter-Diffusion and Self-Diffusion in Solid Lithium
501 Metal. *Phys. Status Solidi B* 38, 559–569. <https://doi.org/10.1002/pssb.19700380206>
- 502 Manceau, A., Schlegel, M.L., Musso, M., Sole, V.A., Gauthier, C., Petit, P.E., Trolard, F., 2000. Crystal
503 chemistry of trace elements in natural and synthetic goethite. *Geochim. Cosmochim. Acta* 64,
504 3643–3661.
- 505 Markl, G., von Blanckenburg, F., Wagner, T., 2006. Iron isotope fractionation during hydrothermal ore
506 deposition and alteration. *Geochimica Et Cosmochimica Acta*, 70(12): 3011-3030.
- 507 Mattielli, N., Rimetz, J., Petit, J., Perdrix, E., Deboudt, K., Flament, P., Weis, D., 2006. Zn Cu isotopic
508 study and speciation of airborne metal particles within a 5-km zone of a lead/zinc smelter.
509 *Geochim. Cosmochim. Acta Suppl.* 70, A401–A401.
- 510 Milot, J., Poitrasson, F., Baron, S., Coustures, M.-P., 2016. Iron isotopes as a potential tool for ancient
511 iron metals tracing. *J. Archaeol. Sci.* 76, 9–20.
- 512 Milot, J., Baron, S., Poitrasson, F., 2018. Potential use of Fe isotopes for ancient non-ferrous metals
513 tracing through the example of a lead-silver production site (Imiter miner, Anti-Atlas,
514 Morocco). *Journal of Archaeological Science*, 98: 22-33.
- 515 Moore, P. (2012). Anglo's new nickel. *International Mining*, March, 20-24.
- 516 Navarro, A., Cardellach, E., Mendoza, J.L., Corbella, M., Domènech, L.M., 2008. Metal mobilization
517 from base-metal smelting slag dumps in Sierra Almagrera (Almería, Spain). *Appl. Geochem.*
518 23, 895–913. <https://doi.org/10.1016/j.apgeochem.2007.07.012>
- 519 Nriagu, J., Pacyna, J., 1988. Quantitative assesment of worldwide contamination of air, water and soils by
520 trace-metals. *Nature* 333, 134–139. <https://doi.org/10.1038/333134a0>
- 521 Ott, A., 1969. Isotope Separation by Thermal Diffusion in Liquid Metal. *Science* 164, 297–297.
522 <https://doi.org/10.1126/science.164.3877.297>
- 523 Oxley, A., Smith, M.E., Caceres, O., 2016. Why heap leach nickel laterites? *Miner. Eng.* 88, 53–60.
- 524 Pi, Q.H., Zhong, R.C., Hu, R.Z., 2015. Tracing the ore-formation history of the shear-zone-controlled
525 Huogeqi Cu-Pb-Zn deposit in Inner Mongolia, northern China, using H, O, S, and Fe isotopes.
526 *Ore Geology Reviews*, 71: 263-272.
- 527 Platzner, I. T., 1997. *Modern isotope ratio mass spectrometry*. Wiley, Chichester, p 514.
- 528 Poitrasson, F., 2006. On the iron isotope homogeneity level of the continental crust. *Chem. Geol.* 235,
529 195–200. <https://doi.org/10.1016/j.chemgeo.2006.06.010>
- 530 Poitrasson, F., Freydier, R., 2005. Heavy iron isotope composition of granites determined by high
531 resolution MC-ICP-MS. *Chem. Geol.* 222, 132–147.
532 <https://doi.org/10.1016/j.chemgeo.2005.07.005>

- 533 Poitrasson, F., Roskosz, M., Corgne, A., 2009. No iron isotope fractionation between molten alloys and
 534 silicate melt to 2000 °C and 7.7 GPa: Experimental evidence and implications for planetary
 535 differentiation and accretion. *Earth Planet. Sci. Lett.* 278, 376–385.
 536 <https://doi.org/10.1016/j.epsl.2008.12.025>
- 537 Poitrasson, F., Delpéch, G., Gregoire, M., 2013. On the iron isotope heterogeneity of lithospheric mantle
 538 xenoliths: implications for mantle metasomatism, the origin of basalts and the iron isotope
 539 composition of the Earth. *Contrib. Mineral. Petrol.* 165, 1243–1258.
 540 <https://doi.org/10.1007/s00410-013-0856-7>
- 541 Poitrasson, F., Vieira, L.C., Seyler, P., dos Santos Pinheiro, G.M., Mulholland, D.S., Bonnet, M.-P.,
 542 Martinez, J.-M., Lima, B.A., Boaventura, G.R., Chmeleff, J., 2014. Iron isotope composition of
 543 the bulk waters and sediments from the Amazon River Basin. *Chem. Geol.* 377, 1–11.
- 544 Poitrasson, F., Viers, J., Martin, F., Braun, J.-J., 2008. Limited iron isotope variations in recent lateritic
 545 soils from Nsimi, Cameroon: implications for the global Fe geochemical cycle. *Chem. Geol.*
 546 253, 54–63.
- 547 Quantin, C., Becquer, T., Rouiller, J.H., Berthelin, J., 2002. Redistribution of metals in a New Caledonia
 548 ferralsol after microbial weathering. *Soil Sci. Soc. Am. J.* 66, 1797–1804.
- 549 Ratié, G., Garnier, J., Calmels, D., Vantelon, D., Guimarães, E., Monvoisin, G., Nouet, J., Ponzevera, E.,
 550 Quantin, C., 2018. Nickel distribution and isotopic fractionation in a Brazilian lateritic regolith:
 551 Coupling Ni isotopes and Ni K-edge XANES. *Geochim. Cosmochim. Acta* 230, 137–154.
- 552 Ratié, G., Jouvin, D., Garnier, J., Rouxel, O., Miska, S., Guimarães, E., Cruz Vieira, L., Sivry, Y., Zelano,
 553 I., Montarges-Pelletier, E., Thil, F., Quantin, C., 2015. Nickel isotope fractionation during
 554 tropical weathering of ultramafic rocks. *Chem. Geol.* 402, 68–76.
 555 <https://doi.org/10.1016/j.chemgeo.2015.02.039>
- 556 Ratié, G., Quantin, C., Jouvin, D., Calmels, D., Ettler, V., Sivry, Y., Vieira, L.C., Ponzevera, E., Garnier,
 557 J., 2016. Nickel isotope fractionation during laterite Ni ore smelting and refining: Implications
 558 for tracing the sources of Ni in smelter-affected soils. *Appl. Geochem.* 64, 136–145.
- 559 Rauch, J.N., Pacyna, J.M., 2009. Earth's global Ag, Al, Cr, Cu, Fe, Ni, Pb, and Zn cycles. *Glob.*
 560 *Biogeochem. Cycles* 23, GB2001. <https://doi.org/10.1029/2008GB003376>
- 561 Seignez, N., Gauthier, A., Bulteel, D., Damidot, D., Potdevin, J.-L., 2008. Leaching of lead metallurgical
 562 slags and pollutant mobility far from equilibrium conditions. *Appl. Geochem.* 23, 3699–3711.
 563 <https://doi.org/10.1016/j.apgeochem.2008.09.009>
- 564 Shiel, A.E., Weis, D., Orians, K.J., 2010. Evaluation of zinc, cadmium and lead isotope fractionation
 565 during smelting and refining. *Sci. Total Environ.* 408, 2357–2368.
 566 <https://doi.org/10.1016/j.scitotenv.2010.02.016>
- 567 Šillerová, H., Chrástný, V., Vítková, M., Francová, A., Jehlička, J., Gutsch, M.R., Kocourková, J.,
 568 Aspholm, P.E., Nilsson, L.O., Berglen, T.F., 2017. Stable isotope tracing of Ni and Cu
 569 pollution in North-East Norway: Potentials and drawbacks. *Environ. Pollut.* 228, 149–157.
- 570 Sivry, Y., Riotte, J., Sonke, J.E., Audry, S., Schäfer, J., Viers, J., Blanc, G., Freydier, R., Dupré, B., 2008.
 571 Zn isotopes as tracers of anthropogenic pollution from Zn-ore smelters The Riou Mort–Lot
 572 River system. *Chem. Geol.* 255, 295–304.
- 573 Sonke, J.E., Sivry, Y., Viers, J., Freydier, R., Dejonghe, L., Andre, L., Aggarwal, J.K., Fontan, F., Dupre,
 574 B., 2008. Historical variations in the isotopic composition of atmospheric zinc deposition from
 575 a zinc smelter. *Chem. Geol.* 252, 145–157. <https://doi.org/10.1016/j.chemgeo.2008.02.006>

- 576 Souto-Oliveira, C.E., Babinski, M., Araújo, D.F., Andrade, M.F., 2018. Multi-isotopic fingerprints (Pb,
577 Zn, Cu) applied for urban aerosol source apportionment and discrimination. *Sci. Total Environ.*
578 626, 1350–1366.
- 579 Souto-Oliveira, C.E., Babinski, M., Araújo, D.F., Weiss, D.J., Ruiz, I.R., 2019. Multi-isotope approach of
580 Pb, Cu and Zn in urban aerosols and anthropogenic sources improves tracing of the
581 atmospheric pollutant sources in megacities. *Atmos. Environ.* 198, 427–437.
- 582 Teixeira, N.L., Caxito, F.A., Rosière, C.A., Pecoits, E., Vieira, L.C., Frei, R., Sial, A.N., Poitrasson, F.,
583 2017. Trace elements and isotope geochemistry (C, O, Fe, Cr) of the Cauê iron formation,
584 Quadrilátero Ferrífero, Brazil: Evidence for widespread microbial dissimilatory iron reduction
585 at the Archean/Proterozoic transition. *Precambrian Research*, 298: 39-55.
- 586 Thompson, A., Ruiz, J., Chadwick, O.A., Titus, M., Chorover, J., 2007. Rayleigh fractionation of iron
587 isotopes during pedogenesis along a climate sequence of Hawaiian basalt. *Chem. Geol.* 238,
588 72–83.
- 589 Wang, Y., Zhu, X.K., Mao, J.W., Li, Z.H., Cheng, Y.B., 2011. Iron isotope fractionation during skarn-
590 type metallogeny: A case study of Xinqiao Cu-S-Fe-Au deposit in the Middle-Lower Yangtze
591 valley. *Ore Geology Reviews*, 43(1): 194-202.
- 592 Warner, A.E.M., Diaz, C.M., Dalvi, A.D., Mackey, P.J., Tarasov, A.V., 2006. JOM world nonferrous
593 smelter survey, part III: Nickel: Laterite. *Jom* 58, 11–20.
- 594 Wasylenki, L. E., Howe, H. D., Spivak-Birndorf, L. J., & Bish, D. L. (2015). Ni isotope fractionation
595 during sorption to ferrihydrite: implications for Ni in banded iron formations. *Chemical*
596 *Geology*, 400, 56-64.
- 597 Wawryk, C.M., Foden, J.D., 2015. Fe-isotope fractionation in magmatic-hydrothermal mineral deposits: A
598 case study from the Renison Sn-W deposit, Tasmania. *Geochimica et Cosmochimica Acta*,
599 150: 285-298.
- 600 Weyer, S., Ionov, D.A., 2007. Partial melting and melt percolation in the mantle: the message from Fe
601 isotopes. *Earth and Planetary Science Letters* 259, 119–133.
- 602 Wiederhold, J.G., 2015. Metal Stable Isotope Signatures as Tracers in Environmental Geochemistry.
603 *Environ. Sci. Technol.* 49, 2606–2624. <https://doi.org/10.1021/es504683e>
- 604 Wiederhold, J.G., Teutsch, N., Kraemer, S.M., Halliday, A.N., Kretzschmar, R., 2007. Iron isotope
605 fractionation in oxic soils by mineral weathering and podzolization. *Geochim. Cosmochim.*
606 *Acta* 71, 5821–5833.
- 607 Wu, B., Amelung, W., Xing, Y., Bol, R., & Berns, A. E., 2019. Iron cycling and isotope fractionation in
608 terrestrial ecosystems. *Earth-science reviews*, 190, 323-352.
- 609 Yamaguchi, K.E., Johnson, C.M., Beard, B.L., Beukes, N.J., Gutzmer, J., Ohmoto, H., 2007. Isotopic
610 evidence for iron mobilization during Paleoproterozoic lateritization of the Hekpoort paleosol
611 profile from Gaborone, Botswana. *Earth Planet. Sci. Lett.* 256, 577–587.
- 612 Yin, N.-H., van Hullebusch, E.D., Benedetti, M., Lens, P.N.L., Sivry, Y., 2018. Zn isotopes fractionation
613 during slags' weathering: One source of contamination, multiple isotopic signatures.
614 *Chemosphere* 195, 483–490. <https://doi.org/10.1016/j.chemosphere.2017.11.184>.
- 615 Zhao, X., Zhang, H., Zhu, X., Tang, S., Tang, Y., 2010. Iron isotope variations in spinel peridotite
616 xenoliths from North China Craton: implications for mantle metasomatism. *Contributions to*
617 *Mineralogy and Petrology* 160, 1–14.

Table captions

Table 1: List of natural and pyrometallurgical samples and their Fe and Zr contents. $\tau_{\text{Fe}} = ([\text{Fe}]/[\text{Zr}]_{\text{sample}} / [\text{Fe}]/[\text{Zr}]_{\text{protolith}} - 1)$, where the sample RC27-28 represents the protolith. The UMIA values are expressed using Eq 2. The Fe isotope composition and two standard errors are calculated from the 3 analyses using Student's t-corrected factor (Platzner, 1997). $\delta\text{Fe}/\text{amu}$ is the deviation of the Fe isotope composition of a sample relative to the standard and normalized to a mass difference of 1 atomic mass unit (amu).

Journal Pre-proof

Sample name	Depth	[Fe]	[Zr]	τ Fe	Al ₂ O ₃	Fe ₂ O ₃	MgO	SiO ₂	UMIA	$\delta^{57}\text{Fe}$	2 SE	$\delta\text{Fe}/\text{amu}$
		<i>g kg⁻¹</i>	<i>mg kg⁻¹</i>		<i>mol kg⁻¹</i>				%	‰		
Soil samples												
BAS1 0-10	0-10 cm	271	14	-0.10	0.56	2.27	2.59	1.97	38.3	-0.10	± 0.07	-0.03
BAS1 10-30	10-30 cm	261	13	-0.09	0.51	2.19	2.06	2.13	39.1	0.02	± 0.15	0.01
BAS1 30-80	30-80 cm	255	13	-0.08	0.71	2.28	3.69	2.13	34.0	0.00	± 0.13	0.00
Lateritic samples												
RC0-1	3-4 m	256	11	0.08	0.15	2.29	0.68	6.05	26.6	0.07	± 0.05	0.02
RC6-7	9-10 m	369	14	0.22	0.28	3.31	0.08	4.47	44.0	-0.06	± 0.11	-0.02
RC16-17	19-20 m	85	4	0.01	0.17	0.76	1.46	4.51	13.5	0.02	± 0.19	0.01
RC24-25	27-28 m	67	3	0.05	0.07	0.60	6.17	4.13	6.1	0.02	± 0.34	0.01
RC27-28	30-31 m	49	2	0.00	0.03	0.43	5.88	4.30	4.4	0.08	± 0.20	0.03
By-products												
Ore 1		165								0.00	± 0.18	0.00
Ore 5		118								0.03	± 0.20	0.01
SS7		106								-0.10	± 0.09	-0.03
SS8		124								0.05	± 0.14	0.02
WRS		71								0.07	± 0.08	0.02
BRS		179								0.05	± 0.11	0.02
FeNi2		689								0.07	± 0.12	0.02

Figure captions

Figure 1: Schematic view of the FeNi smelting and refining processes modified from Ettler et al. (2016) showing the average Ni and Fe contents in ore (n= 7), F (n=10), SS (n=8), WRS (n=1), BRS (n=1) and FeNi (n=2) (Ratié et al., 2016).

Figure 2: Ternary plot showing the molar composition ($\text{Al}_2\text{O}_3+\text{Fe}_2\text{O}_3$, SiO_2 , MgO) and its relationship with the ultramafic index of alteration (UMIA) samples. The yellow arrow shows the general trend of weathering among the plotted samples.

Figure 3: Iron isotope values ($\delta^{57}\text{Fe}$ in ‰) vs. the τ_{Fe} normalized by Zr (Poitrasson et al., 2008; our study), Th (Liu et al., 2014) and Ti (Li et al., 2017). The blue band represents the $\delta^{57}\text{Fe}$ value of the bulk silicate Earth (Poitrasson et al., 2006).

Figure 4: $\delta\text{Ni}/\text{amu}$ and $\delta\text{Fe}/\text{amu}$ values for the lateritic profile, ultramafic (UM) soils, and products from mining (feed material) and smelting (smelting slags, refining slags, and FeNi) activities. $\delta\text{Ni}/\text{amu}$ values were calculated based on the $\delta^{60/58}\text{Ni}$ values in Ratié et al. (2015, 2016, 2018). The green band represents the $\delta\text{Ni}/\text{amu}$ value of the bulk silicate Earth (Gall et al., 2017) and the blue band represents the $\delta\text{Fe}/\text{amu}$ value of the bulk silicate Earth (Poitrasson, 2006). The dotted line separates anthropogenic samples from geogenic samples.

Figure 5: Iron isotopic composition vs. the inverse Fe concentration (g/kg). The blue area represents the mean $\delta^{57}\text{Fe}$ value of the whole Barro Alto complex ($0.01 \pm 0.11\text{‰}$). The orange arrow represents the range of $\delta^{57}\text{Fe}$ values for non-ultramafic soils (Wu et al., 2019).

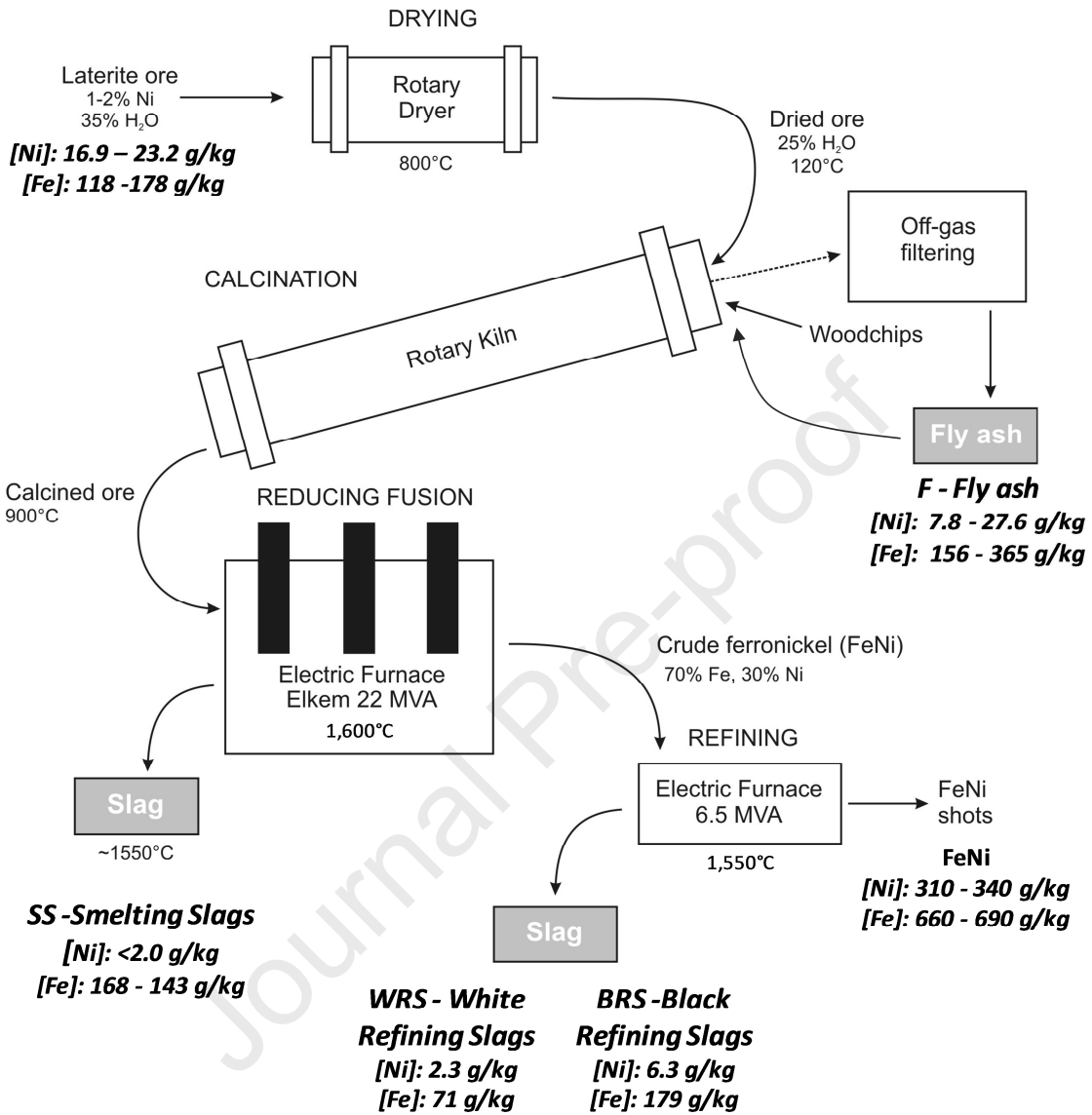


Figure 1

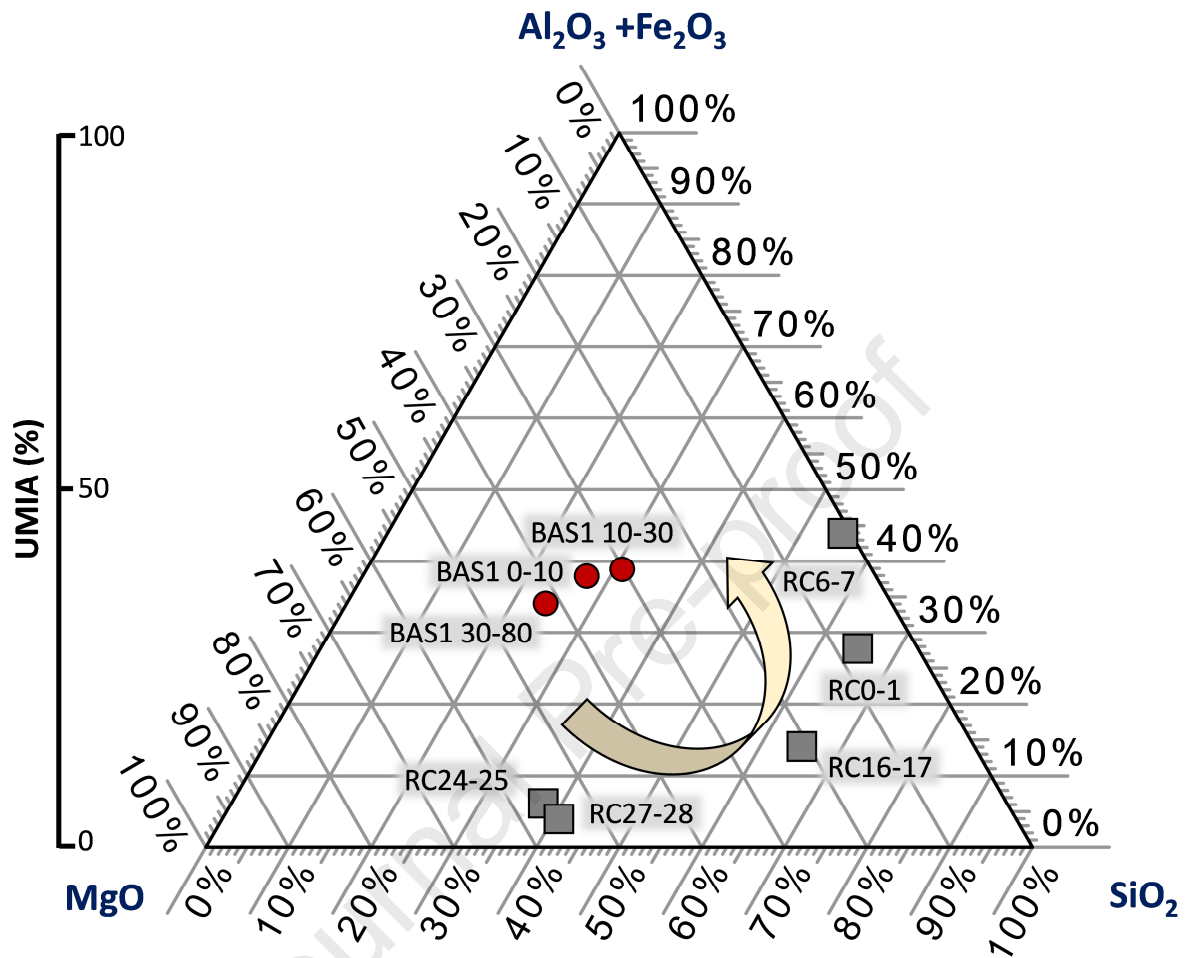


Figure 2

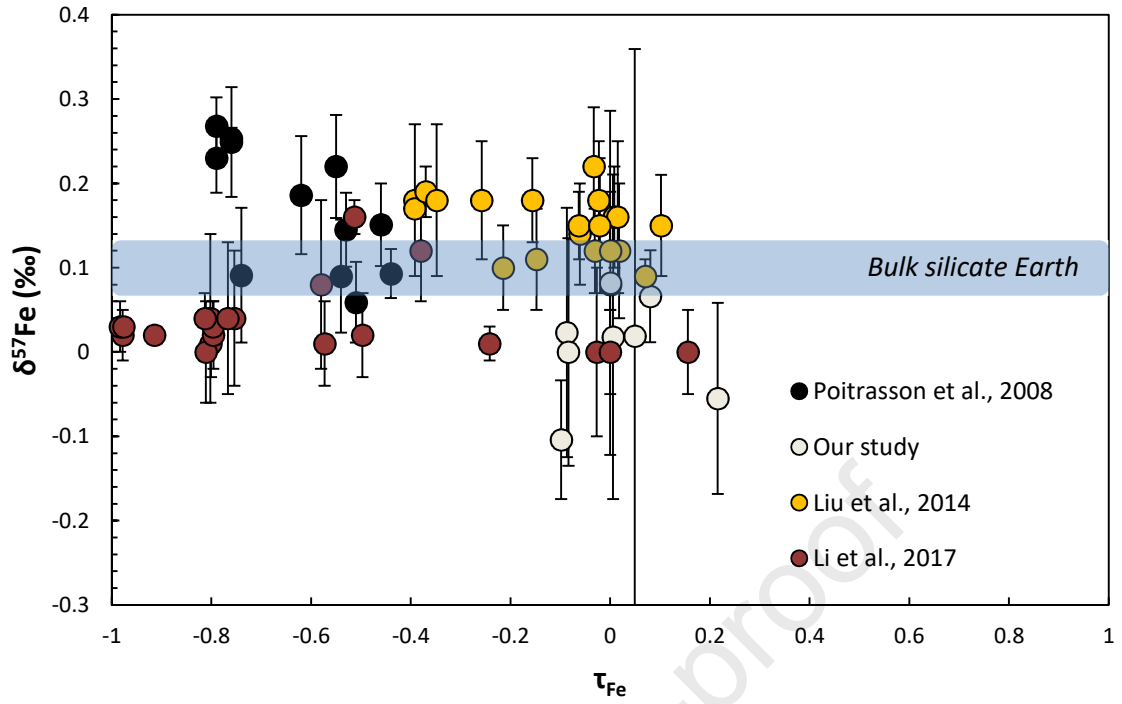


Figure 3

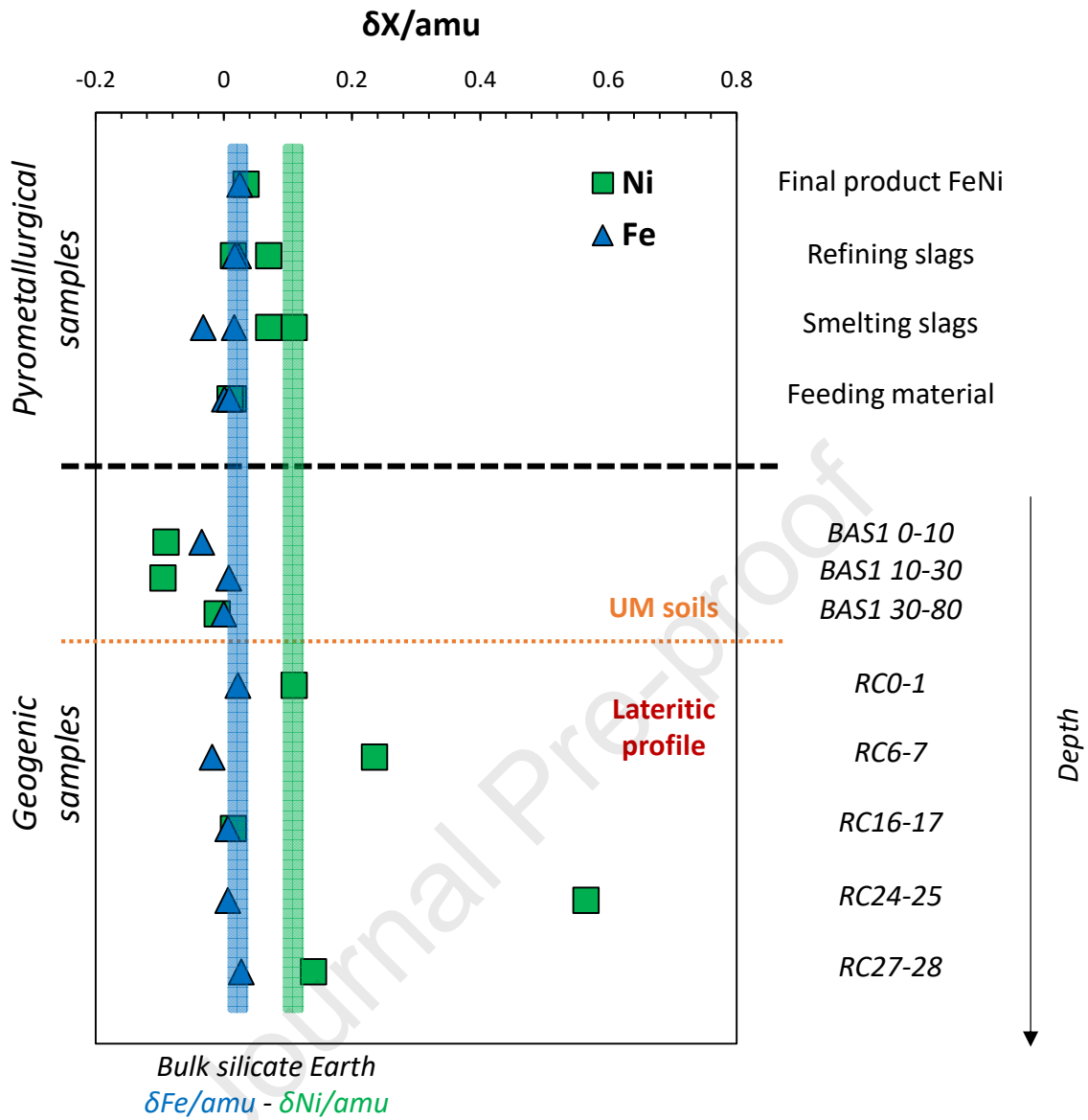


Figure 4

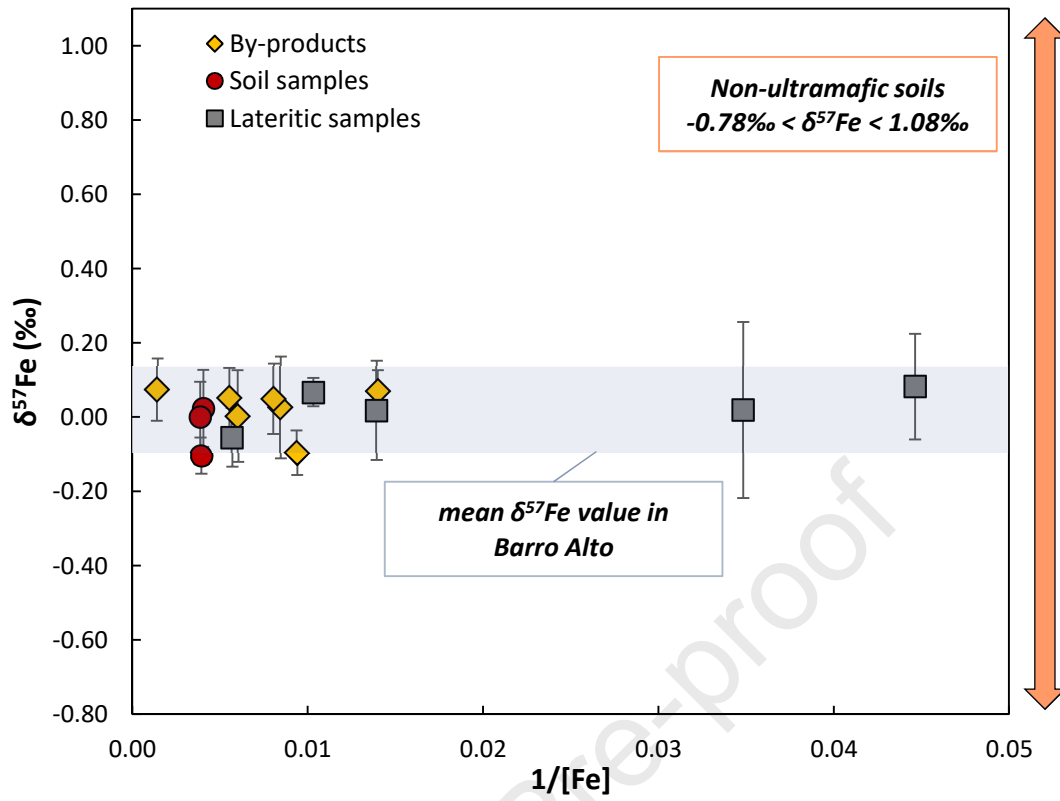


Figure 5

Investigation of Fe isotope systematics for the complete sequence of natural and metallurgical processes of Ni lateritic ores: Implications for environmental source tracing

*Gildas Ratié¹, Jérémie Garnier², Lucieth Cruz Vieira², Daniel F. Araújo³, Michael Komárek¹,
Franck Poitrasson⁴, Cécile Quantin⁵*

Highlights

- Fe mobility does not induce isotopic fractionation during chemical weathering.
- There is no evidence of Fe isotope fractionation during the RKEF smelting process.
- Smelting slags are stamped with $\delta^{57}\text{Fe}$ values from Ni laterite ores.
- The use of Fe isotopes as an environmental tracer in lateritic soils is limited.
- Fe isotopes may be a potential tracer of mining activities in non-lateritic soils.

Declaration of interests

The authors declare that they have no known competing financial interests or personal relationships that could have appeared to influence the work reported in this paper.

The authors declare the following financial interests/personal relationships which may be considered as potential competing interests:

Journal Pre-proof